J. Fluid Mech. (1985), *vol.* 151, *pp.* 427–442
Printed in Great Britain

Measurements of the wind-wave energy flux in an opposing wind

By IAN R. YOUNG†
Max-Planck-Institut für Meteorologie, D-2000 Hamburg 13, West Germany
AND RODNEY J. SOBEY
Department of Civil Engineering, University of California, Berkeley, CA 94720, U.S.A.

(Received 20 September 1983 and in revised form 10 August 1984)

A wind-wave flume which allows mechanically generated water waves to propagate in opposition to a boundary-layer air flow has been used to measure the air-flow structure in an opposing wind–wave situation. Measurements of the wave-induced pressure closely follow the predictions of potential flow theory, with the pressure in antiphase with the water surface. Hence, in contrast to the following wind situation, there is no appreciable air–water energy flux due to normal stresses. The vertical and horizontal wave-induced velocities deviate slightly in magnitude from the potential flow result while still following it qualitatively. Based on these velocity measurements it is determined that the Reynolds stress $-\rho_a \widetilde{u}\widetilde{u}$ is the dominant term in causing the decay of waves in opposing winds. The predicted rate of decay has a squared dependence on the wave slope and the ratio of wind speed to wave phase speed.

1. Introduction

Considerable attention has been focused in recent decades on the processes responsible for initiation and growth of water waves. The particular theoretical predictions of Miles (1957, 1959, 1960, 1962, 1967) and Phillips (1957) have been extensively investigated in the laboratory (Shemdin 1969; Wu, Hsu & Street 1977; Chao & Hsu 1978; Hsu, Hsu & Street 1981) and in the field (Dobson 1971; Elliott 1972; Snyder 1974; Snyder *et al.* 1981). Although these measurements are to some extent contradictory to each other and to the theory, the relevant physical processes are now reasonably well understood, at least in a qualitative sense.

In contrast, wind–wave interaction under an opposing wind has received little attention. Such situations are not especially common but they are potentially significant in complex wind fields such as tropical cyclones and strong frontal systems. Accurate wave predictions in such situations require some understanding of the response of waves to an opposing wind. This paper describes an experimental investigation of this aspect of air–sea interaction.

2. The air–water energy flux

Phillips (1977) has shown that for a water surface defined by

$$\eta = a\cos(kx - \omega t), \tag{1}$$

where η is the water surface elevation, a the wave amplitude, k the wavenumber and ω the wave angular frequency, an air–water energy flux can result from a surface

† Present address: Department of Civil and Systems Engineering, James Cook University, Townsville, Qld 4811, Australia.

stress of frequency ω. This stress can be either a normal stress $\tilde{\sigma}$ or a shear stress $\tilde{\tau}$, where the tilde indicates a wave-induced quantity with frequency ω. In addition, Longuet-Higgins (1969) has shown that a fluctuating tangential stress applied at the free surface is dynamically equivalent to a normal stress fluctuation of the same magnitude, lagging $\frac{1}{2}\pi$ in phase behind the tangential stress. If the wave-induced stresses are represented as

$$\tilde{\sigma} = (\nu_1 + \mathrm{i}\mu_1)\,\rho_{\mathrm{w}}\,C^2 k\eta \tag{2}$$

and

$$\tilde{\tau} = (\nu_2 + \mathrm{i}\mu_2)\,\rho_{\mathrm{w}}\,C^2 k\eta, \tag{3}$$

then the effective normal stress at the water surface is

$$\tilde{\sigma}_{\mathrm{e}} = (\nu + \mathrm{i}\mu)\,\rho_{\mathrm{w}}\,C^2 k\eta, \tag{4}$$

where $\nu = \nu_1 - \mu_2$ and $\mu = \mu_1 + \nu_2$ are coupling coefficients which are in practice both small, $|\nu|, |\mu| \ll 1$.

For a progressive wavetrain, the rate of working (or energy flux) by the effective normal stress is (Phillips 1977)

$$\frac{\partial E}{\partial t} = \overline{\tilde{\sigma}_{\mathrm{e}} \frac{\partial \eta}{\partial t}}, \tag{5}$$

which involves specifically that component of effective normal stress in quadrature with the water surface. From (4) and (5) the energy flux is

$$\frac{\partial E}{\partial t} = \mu \omega E, \tag{6}$$

the coupling coefficient $\mu = \mu_1 + \nu_2$ determining the rate of the air–water energy flux. Representing the wave-induced surface stresses as

$$\tilde{\sigma} = \mathrm{amp}\,(\tilde{\sigma})\cos(kx - \omega t + \phi) \tag{7}$$

and

$$\tilde{\tau} = \mathrm{amp}\,(\tilde{\tau})\cos(kx - \omega t + \phi), \tag{8}$$

where the terminology amp ( ) indicates the amplitude of the quantity in brackets, leads to the following expressions for the components of the coupling coefficient μ:

$$\mu_1 = \frac{-\mathrm{amp}\,(\tilde{\sigma})\sin\phi}{\rho_{\mathrm{w}}\,C^2 ka} \tag{9}$$

and

$$\nu_2 = \frac{\mathrm{amp}\,(\tilde{\tau})\cos\phi}{\rho_{\mathrm{w}}\,C^2 ka}. \tag{10}$$

Simultaneous measurements of water-surface elevation and surface wave-induced stress will define μ_1 and ν_2 and hence the air–water energy flux.

The components of the $\tilde{\sigma}$ and $\tilde{\tau}$ surface stresses can be determined from the conservation equations of mass and momentum. In tensor notation, the conservation form of the momentum equation is

$$\rho_{\mathrm{a}}\left[\frac{\partial u_i}{\partial t} + \frac{\partial}{\partial x_j}(u_i u_j)\right] = \rho_{\mathrm{a}} g_i + \frac{\partial \sigma_{ij}}{\partial x_j}, \tag{11}$$

where ρ_{a} is the air density, $u_i(x_i, t)$ is the instantaneous velocity in the x_i direction and $\sigma_{ij}(x_i, t)$ is the instantaneous stress tensor, in which σ_{ii} is the negative of the static pressure. The pressure $p(x_i, t)$ can be expressed as

$$p = \bar{p} + \tilde{p} + p', \tag{12}$$

where $\bar{p}(x_i)$ is the time-averaged pressure, $\tilde{p}(x_i, t)$ the wave-induced pressure with frequency ω and $p'(x_i, t)$ the uncorrelated turbulent residual. The velocities can be represented in a similar manner:

$$u_i = \bar{u}_i + \tilde{u}_i + u_i' \tag{13}$$

with a decomposition as in (12). Substitution into (11) and time-averaging yields

$$\rho_a\left[\frac{\partial \bar{u}_i}{\partial t} + \frac{\partial}{\partial x_j}(\bar{u}_i \bar{u}_j)\right] = \rho_a g_i + \frac{\partial}{\partial x_j}(\sigma_{ij} - \overline{\tilde{u}_i \tilde{u}_j} - \overline{u_i' u_j'}), \tag{14}$$

which has the same form as (11). The additional 'stress' terms which appear on the right-hand side of (14) are the well-known Reynolds stresses. In conventional turbulence analysis the wave-induced component $\tilde{u}_i$ in (13) is not considered as a separate component, in which case

$$u_i'' = \tilde{u}_i + u_i', \tag{15}$$

where u_i'' is the fluctuating component of velocity. Using this terminology, the Reynolds stress terms become

$$\overline{u_i'' u_j''} = \overline{\tilde{u}_i \tilde{u}_j} + \overline{u_i' u_j'}, \tag{16}$$

where $-\rho_a \overline{u_i'' u_j''}$ is the Reynolds stress; the component $-\rho_a \overline{\tilde{u}_i \tilde{u}_j}$ is the wave-induced Reynolds stress and the component $-\rho_a \overline{u_i' u_j'}$ is the turbulent Reynolds stress.

By definition, the wave-induced pressure $\tilde{p}$ will be normal to the water surface but experimental constraints invariably allow measurements of stress components only in a rectangular cartesian x (horizontal), z (vertical) coordinate system. These measured stress components must be transformed into the orthogonal curvilinear system in the water surface, after which (9) and (10) become (Young 1983)

$$\mu_1 = \Big[-\mathrm{amp}\,(\tilde{p}) \sin\phi_{\tilde{p}\eta} - \mathrm{amp}\left(\frac{\partial \eta}{\partial x}\right)\rho_a \overline{u'' u''} - \mathrm{amp}\left(\frac{\partial \eta}{\partial x}\right)\rho_a \overline{u'' w''} + \mathrm{amp}\left(\frac{\partial \eta}{\partial x}\right) 2\mu \frac{\partial \bar{u}}{\partial x} + \mathrm{amp}\left(\frac{\partial \eta}{\partial x}\right)\mu_a\left(\frac{\partial \bar{w}}{\partial x} + \frac{\partial \bar{u}}{\partial z}\right)\Big] \Big/ \rho_w C^2 k a, \tag{17}$$

$$\nu_2 = 0, \tag{18}$$

where $\phi_{\tilde{p}\eta}$ is the phase difference between $\tilde{p}$ and η, μ_a is the dynamic viscosity of air, and u and w are the velocities in the x and z directions respectively. The first term of (17) represents the energy flux contribution due to normal stresses, the second and third terms represent the effects of Reynolds stresses while the final two terms are viscous stress contributions.

3. Experimental facility and instrumentation

Experiments were conducted in a wind-wave flume of length 14 m, width 0.41 m and height 1.29 m. In all experiments the water depth was 0.32 m. At one end of the flume was an inclined-wedge servo-controlled wavemaker, which was controlled by a PDP-11 minicomputer and could generate any desired wave record. Waves were absorbed at the other end of the flume by an inclined beach. A large centrifugal fan delivered air to this end of the flume through a system of ducting. The fan was driven by an electric motor through a variable-speed transmission, allowing a continuous variation in the flume wind speed from 0 to 7 m s^{-1}.

Correct dynamic scaling between laboratory and field conditions requires equality of both Froude and Reynolds numbers. Cermak (1971), however, has indicated that

the Reynolds number does not have a major influence on the atmospheric boundary layer, the significant flow features being only weakly Reynolds number dependent, provided the flow is turbulent. For Froude scaling and a geometric scale ratio of 50, an ocean wave with height $H = 4$ m and cyclic frequency $f = 0.1$ Hz in a 20 m s^{-1} wind would be modelled by a laboratory wave with $H = 80$ mm and $f = 0.7$ Hz in an air flow of 2.8 m s^{-1}.

The requirements of geometric similitude are particularly relevant in modelling the marine atmospheric boundary layer. Special attention must be given to the boundary-layer shape and to the structure of the longitudinal velocity spectrum E_{uu}. Except very close to the ocean surface, the mean flow in the marine atmospheric boundary layer is described by the log-linear relationship

$$\frac{\bar{u}}{u_*} = \frac{1}{\kappa}\ln\left(\frac{zu_*}{\nu}\right) + C_1, \tag{19}$$

where u_* is the shear velocity, $\kappa \approx 0.4$ is von Kármán's constant, ν is the kinematic viscosity of air and C_1 is a constant. The turbulent structure is also significant, particularly the high-frequency range of the longitudinal velocity spectrum where (Simiu & Scanlan 1978)

$$E_{uu}(f) \propto f^{-\frac{5}{3}}. \tag{20}$$

A series of grids, surface-roughness elements and a fence were installed at the beach end of the flume to achieve a uniform air flow in the cross-flume direction and to thicken the boundary layer. The resulting boundary-layer profile and the longitudinal velocity spectrum measured at a station 2.7 m downstream from the wave-absorbing beach for a free-stream wind velocity of 4.7 m s^{-1}, are shown in figures 1 (*a*) and 1 (*b*) respectively. Equation (19) is also shown in figure 1 (*a*) with u_* and C_1 determined from a least-squares curve fit to the data, u_* being 0.15 ± 0.02 m s^{-1}, where the error represents the 95% confidence limits. This scales to a field value of $u_* = 1.06 \pm 0.14$ m s^{-1}. The free-stream wind velocity of 4.7 m s^{-1} scales to a field value of 33.4 m s^{-1}, with corresponding u_* values of order 1.0 m s^{-1} (Amorocho & De Vries 1980), in good agreement with the laboratory measurements. The measured longitudinal velocity spectrum for the same flow is presented in figure 1 (*b*) and reproduces the $f^{-\frac{5}{3}}$ slope predicted by (20). The satisfactory reproduction of both the shape and turbulent structure of the boundary layer allows the extrapolation of the results to field conditions.

Considerable care was taken to compensate for any spurious effects introduced by the laboratory facility. Both the fan and the flume were mounted on anti-vibration supports and the ducting between them was separated by a rubber gusset to achieve vibration isolation of the flume from both the fan and the laboratory floor. Measurements of the free-stream air flow over the full range of working wind velocities showed no evidence of acoustic disturbances (e.g. from fan vibration) that might contaminate subsequent measurements of wave-induced pressures.

The water-surface time history was measured by a twin-wire resistance wave gauge. Static pressure was measured by a combination of disk, total head and free-stream static pressure probes as calibration of the disk probe revealed that the pressure it sensed was a function of the air velocity. The full probe assembly was calibrated for pitch and yaw, revealing that changes in the angle of the air flow due to the wavy water surface would have an insignificant effect on the measured static pressure.

Both the magnitude of the wave-induced pressure and its phase angle relative to the water waves are critical in determining the air–water energy flux. The dynamic

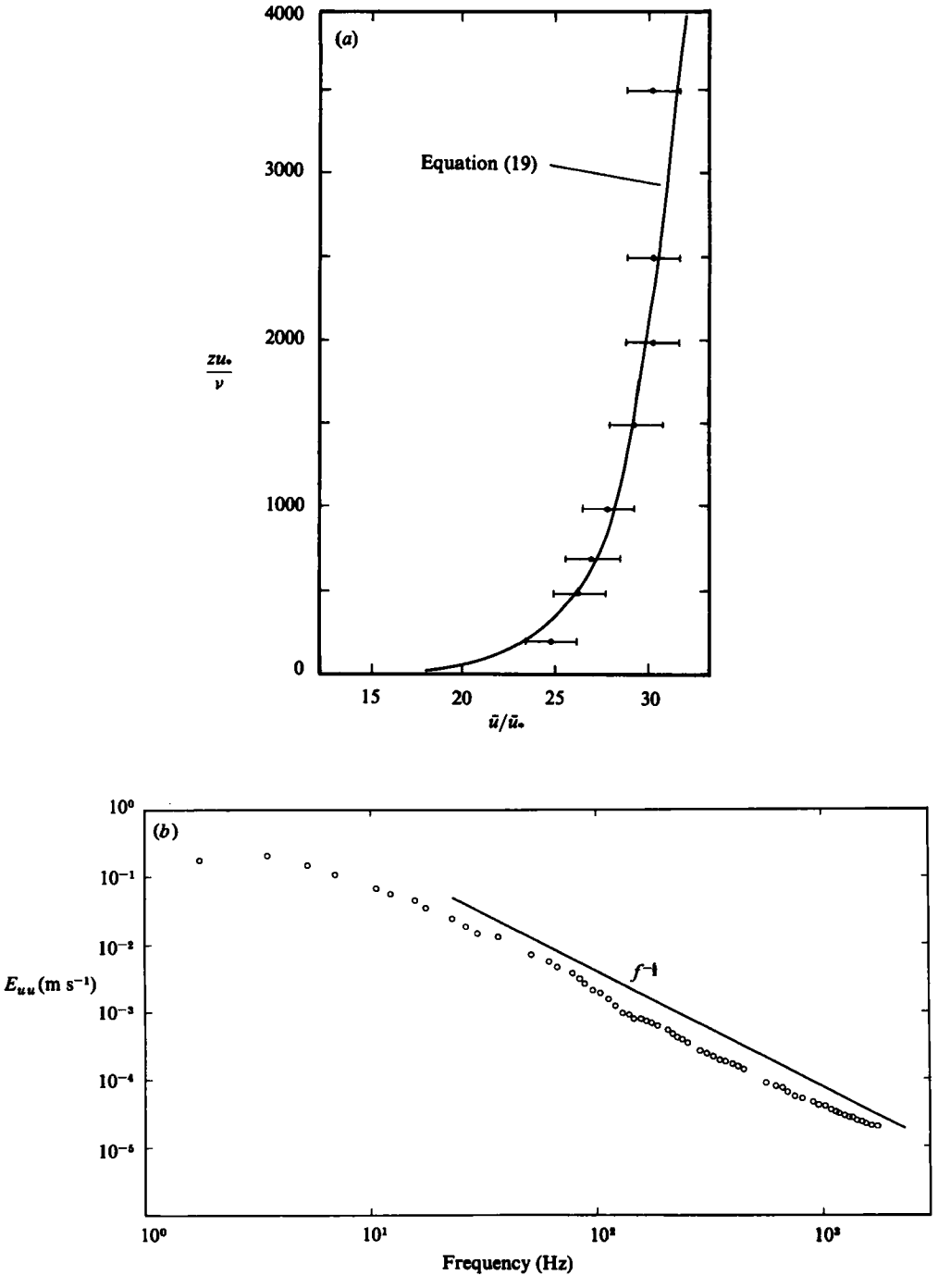

FIGURE 1. (*a*) Mean velocity profile at the beach end of the flume. (*b*) Longitudinal velocity spectrum at the beach end of the flume.

response of the thin pressure lines connecting the pressure probes to the pressure transducers has a potentially major impact on these measurements and was given detailed attention. A dynamic calibration system was constructed which allowed a known oscillatory pressure to be applied to the pressure probes, facilitating the determination of the transfer functions for the pressure lines. These transfer functions were subsequently used to correct the pressure records for the dynamic effects of the tubing.

The Reynolds stress measurements utilized a conventional boundary-layer cross-hot-film anemometer. Both the pressure probes and the hot-film probe were mounted on a wave-follower, allowing all probes to be held a constant distance above the moving water surface. The measured transfer function for the wave-follower confirmed that it followed the water surface with negligible amplitude and phase errors within the frequency range of interest in the experiments. The vertical motion of the wave-follower, however, accelerated the columns of air in the pressure tubing and induced a dynamic pressure in the lines. The magnitude and phase of these effects were measured independently and the recorded pressure signals were adjusted accordingly. The transfer functions of all the electronic systems were also measured and subsequently used to correct the recorded data. All data was recorded on-line to the minicomputer.

4. Data analysis

The calibration curves for the pressure transducers and hot-film probes were determined before and after each set of experiments and used to reduce the recorded data. This data was then corrected for the various system and instrumentation responses described above. The data-reduction methodology is shown schematically in figure 2. This analysis yielded time series of p, u_i and η, which were decomposed into time-averaged, wave-induced and turbulent components as described by (12) and (13).

The time-averaged component of any general flow quantity $r(x_i, t)$ is

$$\bar{r}(x_i) = \frac{1}{2N+1} \sum_{n=-N}^{N} r(x_i, t). \tag{21}$$

Hsu *et al.* (1981) have extracted the wave-induced component $\tilde{r}(x_i, t)$ as

$$\tilde{r}(x_i, t) = \langle r(x_i, t) \rangle - \bar{r}(x_i), \tag{22}$$

where $\langle r(x_i, t) \rangle$ is a phase-averaged term, defined by

$$\langle r(x_i t) \rangle = \frac{1}{2N+1} \sum_{n=-N}^{N} r(x_i, t+n\tau), \tag{23}$$

and τ is the period of the organized oscillation. The time series $\tilde{r}(x_i, t)$ obtained from (22) and (23) will contain, in addition to the wave-induced component, all its higher harmonics. To avoid the inclusion of such harmonics, an alternative approach was adopted. The time series $r(x_i, t)$ was filtered using a non-recursive digital bandpass filter, the pass band being centred about the frequency of the organized oscillation. Such filters can be designed with almost ideal filter characteristics and the pass band can be very narrow, resulting in an accurate determination of $\tilde{r}(x_i, t)$. The turbulent component can then be obtained as

$$r'(x_i, t) = r(x_i, t) - \bar{r}(x_i) - \tilde{r}(x_i, t). \tag{24}$$

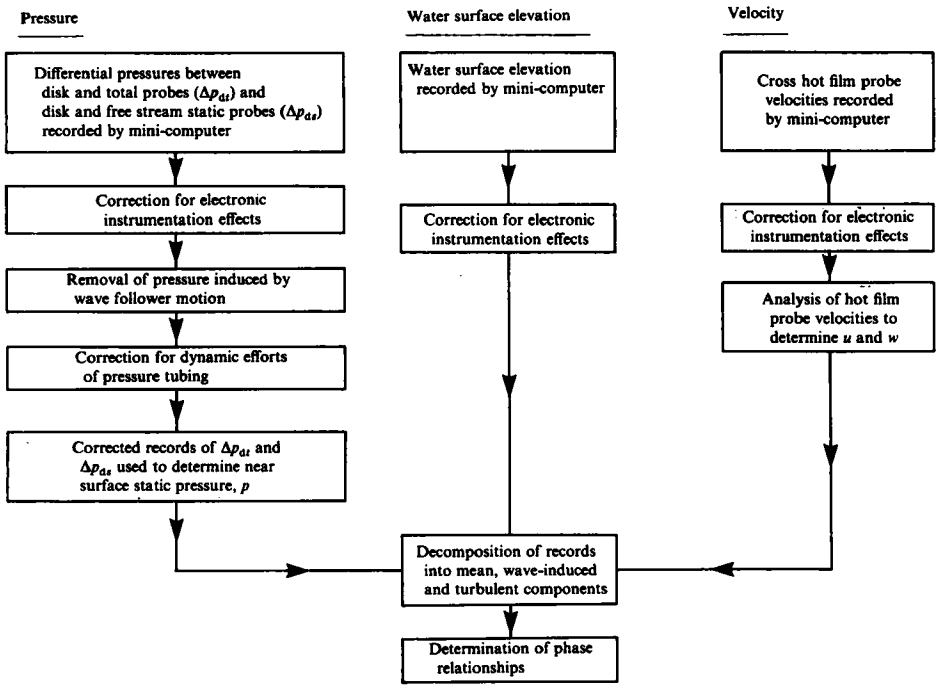

FIGURE 2. Data-reduction methodology.

A detailed description of the experimental facility, instrumentation and data analysis procedures has been presented by Young (1983).

The determination of a time-averaged quantity $\bar{r}(x_i)$ for $z < a$ (where a is the wave amplitude and z is the fixed measuring height) becomes meaningless since the fixed position x_i is sometimes in the water and sometimes in the air. The position of the point relative to the moving water surface is a function of the wave phase. This problem can be overcome by transforming the fixed coordinate system into a wave-following coordinate system. Such a transformation can be written as

$$t^* = t, \quad x^* = x, \quad y^* = y, \quad z^* = z + f(z)\,\eta,$$

where the asterisk notation indicates a fixed co-ordinate system and η is given by (1). It follows that an experimental probe need only be oscillated vertically to always lie at a constant x, y, z point. The only remaining problem is the specification of the weighting function $f(z)$.

Both Phillips (1977) and Hsu *et al.* (1981) have indicated that, since the wave-induced pressure and velocity fields decay with height above the water surface, $f(z)$ should satisfy the boundary conditions $f(0) = 1$ and $f(\infty) = 0$. Shemdin (1969), Dobson (1971), Chao & Hsu (1978) and Snyder *et al.* (1981) have all neglected the upper boundary condition $f(\infty) = 0$ and have assumed $f(z) = 1$ for all values of z. This assumption greatly reduces the complexity of the wave-follower required. Snyder *et al.* (1981) have considered this simplification in some detail and concluded that, for practical measurements, the error introduced is not significant. The wave-follower used here was of this type, keeping the probes a fixed distance above the water surface, irrespective of height. Some indication of the possible bias introduced can be seen by examining the magnitude of the decay of the wave-induced pressure and

velocity fields as a function of z. Both potential flow theory (Lamb 1932) and field measurements (Snyder *et al.* 1981) indicate that these quantities are a function of e^{-kz}. Hence, for a wave of frequency 1 Hz (typical for the present experiments) the wave-induced quantities would only attenuate to 70% of their water-surface values ($z = 0$) at a height of 120 mm, the maximum measurement height used. It is believed that such an effect would produce little error in the results.

5. Surface pressure field

The wave-induced pressure field was determined from a total of 336 pressure experiments. These measurements were made for wave frequencies of $f = 0.75$, 1.00, 1.25, 1.50, 1.75 and 2.00 Hz, probe heights above the moving water surface of $z = 20$, 35, 63, and 120 mm and free-stream wind velocities U_∞ between 0 and 6 m s^{-1}. From the recorded time series, the amplitude of the wave and pressure signals and their phase relationship were determined. A typical example of the simultaneously recorded time series, η and p, is shown in figure 3.

The phase angle between the pressure and water-surface elevations is critical in determining the energy flux and this parameter is presented in figure 4 as a function of U_∞/C. Although there is some scatter in the data, the phase angle appears to be constant at $183° \pm 6°$, where the error represents the 95% confidence interval. This result is consistent with the potential flow solution (Lamb 1932), which predicts

$$\frac{\text{amp}\,(\tilde{p})}{\rho_a g} = -a\,e^{-kz}\left(1-\frac{U_\infty}{C}\right)^2, \tag{25}$$

the negative sign indicating that the pressure is 180° out of phase with the water surface. The amplitude of the measured wave-induced pressures are presented in figure 5 as a function of the potential flow solution. The data follows a clear linear trend which falls slightly below the potential flow solution. A least-squares approximation yields

$$\frac{\text{amp}\,(\tilde{p})}{\rho_a g} = (0.8 \pm 0.2)\,a\,e^{-kz}\left(1-\frac{U_\infty}{C}\right)^2, \tag{26}$$

where the error again represents the 95% confidence interval. The potential flow prediction does lie within these bounds but some divergence from (25) is not unexpected because of real fluid behaviour, although potential flow predictions of pressure in steady-flow boundary layers are often quite successful.

6. Surface velocity field

The velocity field was determined from a total of 264 experiments covering the same range of wind speed and wave frequency as the pressure experiments. Measurement elevations were $z = 30$, 55, 77 and 100 mm. A typical example of the simultaneously recorded time series of η, u and w is shown in figure 6. The cross-film data was analysed to yield time series of the horizontal velocity u and the vertical velocity w. Removing the means from this data leaves the oscillating components

$$u'' = \tilde{u} + u', \tag{27}$$

and

$$w'' = \tilde{w} + w', \tag{28}$$

which were digitally bandpass filtered to determine the wave-induced components

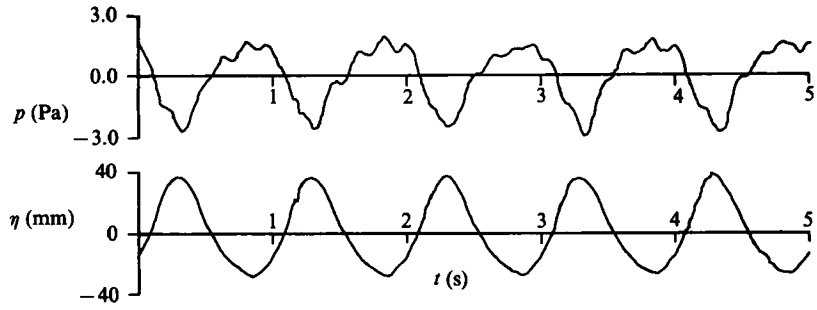

FIGURE 3. Typical time histories of water-level elevation and air pressure for $U_\infty = -3$ m s^{-1}, $f = 1.0$ Hz and $z = 20$ mm.

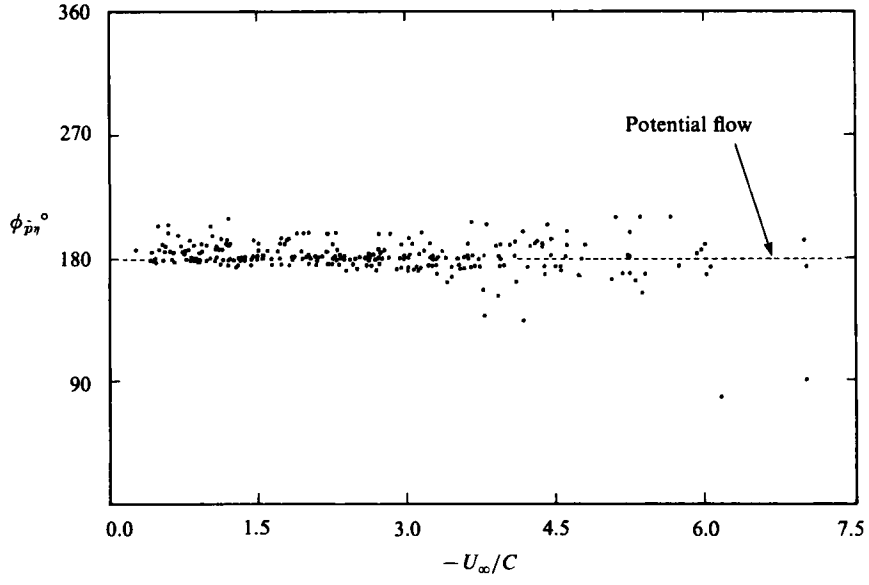

FIGURE 4. The phase angle between the water-level elevation and the wave-induced pressure as a function of U_∞/C.

$\tilde{u}$ and $\tilde{w}$. The phase angles between the wave-induced velocities and the waves, $\phi_{\tilde{u}\eta}$ and $\phi_{\tilde{w}\eta}$, are presented as a function of U_∞/C in figure 7. There is some scatter but both data sets appear to be constant across the full range of U_∞/C values. The mean values of $\phi_{\tilde{u}\eta} = 186°$ and $\phi_{\tilde{w}\eta} = 86°$ compare favourably with the potential flow predictions of $\phi_{\tilde{u}\eta} = 180°$ and $\phi_{\tilde{w}\eta} = 90°$. Potential flow also predicts that the amplitudes of the wave-induced velocities should follow the relationship

$$\text{amp}\,(\tilde{u}) = \text{amp}\,(\tilde{w}) = a(\omega - kU_\infty)\,\mathrm{e}^{-kz}. \tag{29}$$

Figure 8 presents the measured amplitudes of $\tilde{u}$ and $\tilde{w}$ as a function of the potential flow solution; the agreement is again excellent except for the reduced magnitude.

Each of the Reynolds stress terms in (17) has two components: a wave-induced Reynolds stress and a turbulent Reynolds stress (see (16)). Except at low velocities, spectral analysis consistently showed that $\overline{u_i' u_j'} \ll \overline{\tilde{u}_i \tilde{u}_j}$. In addition the wave-induced Reynolds stresses can be determined from the potential flow solutions, which again

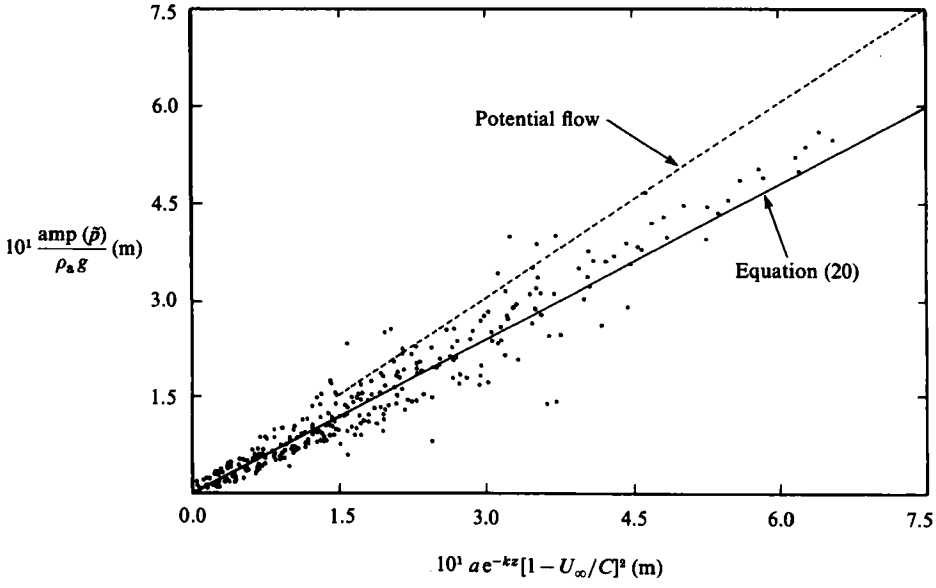

FIGURE 5. The amplitude of the wave-induced pressure as a function of the potential flow solution.

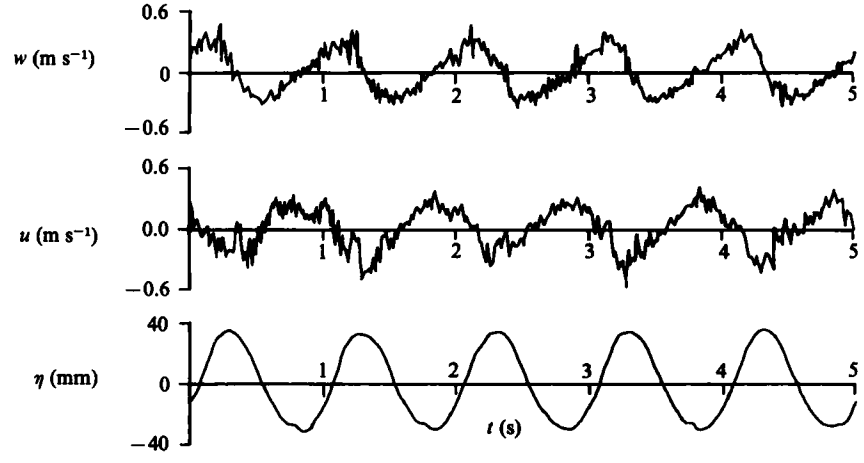

FIGURE 6. Typical time histories of water-level elevation and the horizontal and vertical components of velocity for $U_\infty = -3$ m s^{-1}, $f = 1.0$ Hz and $z = 30$ mm.

provide reasonable descriptions of the trends in the experimental data. As a first approximation, the Reynolds stress terms may be represented as

$$\overline{u''u''} \approx \tfrac{1}{2}K_1[a(\omega - kU_\infty)\,e^{-kz}]^2, \tag{30a}$$

$$\overline{w''w''} \approx \tfrac{1}{2}K_2[a(\omega - kU_\infty)\,e^{-kz}]^2 \tag{30b}$$

and

$$\overline{u''w''} \approx 0, \tag{30c}$$

where K_1 and K_2 are constants of proportionality which would be 1.0 if the flow agreed exactly with potential theory. The cross Reynolds stress $\overline{u''w''}$ is zero since $\tilde{u}$ and $\tilde{w}$

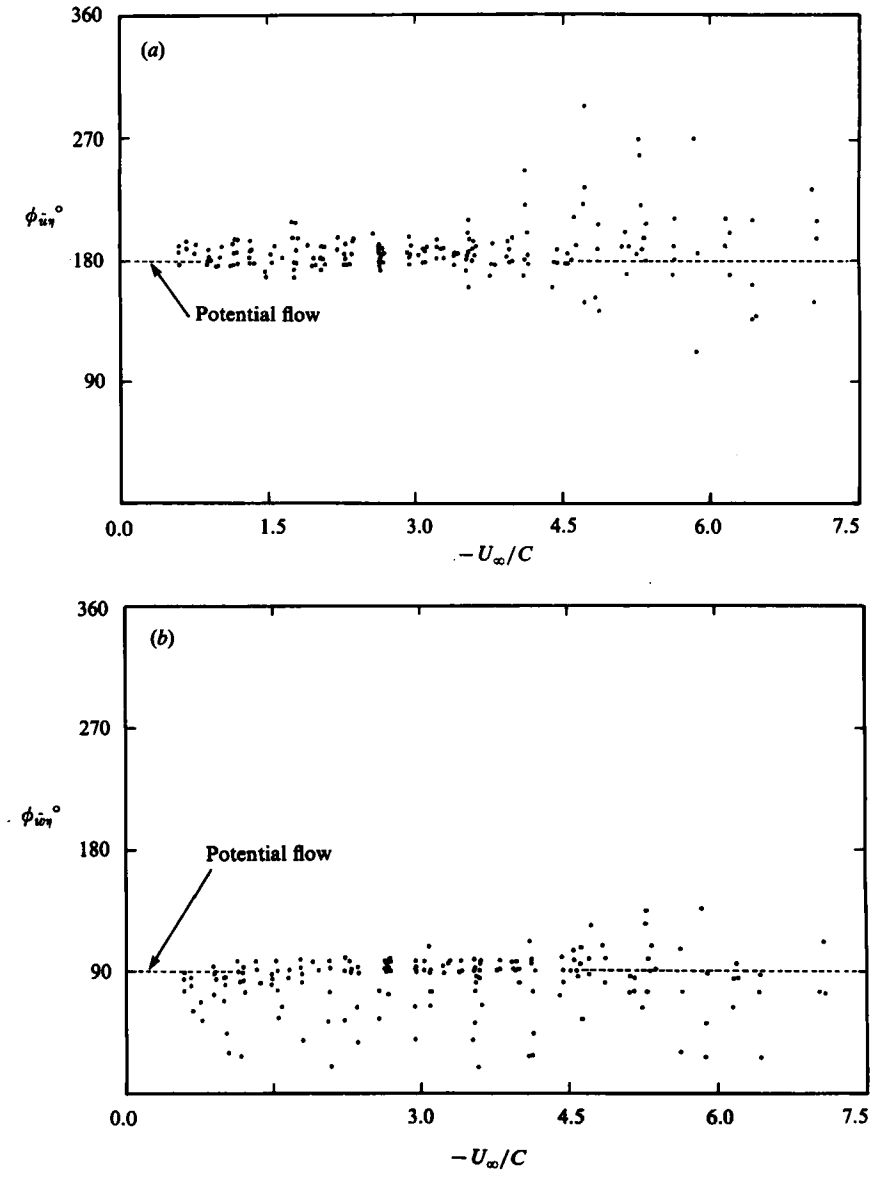

FIGURE 7. (*a*) The phase angle between the water-level elevation and the horizontal component of wave-induced velocity as a function of U_∞/C. (*b*) The phase angle between the water-level elevation and the vertical component of wave-induced velocity as a function of U_∞/C.

are 90° out of phase. The measured Reynolds stress terms are plotted in figure 9 and indicate that (30*a*, *b*, *c*) are reasonable approximations with $K_1 = 1.4 \pm 0.4$ and $K_2 = 0.4 \pm 0.2$.

The relative agreement of the potential flow predictions with the present experiments is rather surprising when it is recognized that the measurements are all in the turbulent boundary layer. It may be that this occurs for no other reason than that the potential flow predictions are dimensionally correct. Other dimensionless presentations were attempted but none of these collapsed the data to such recognizable trends.

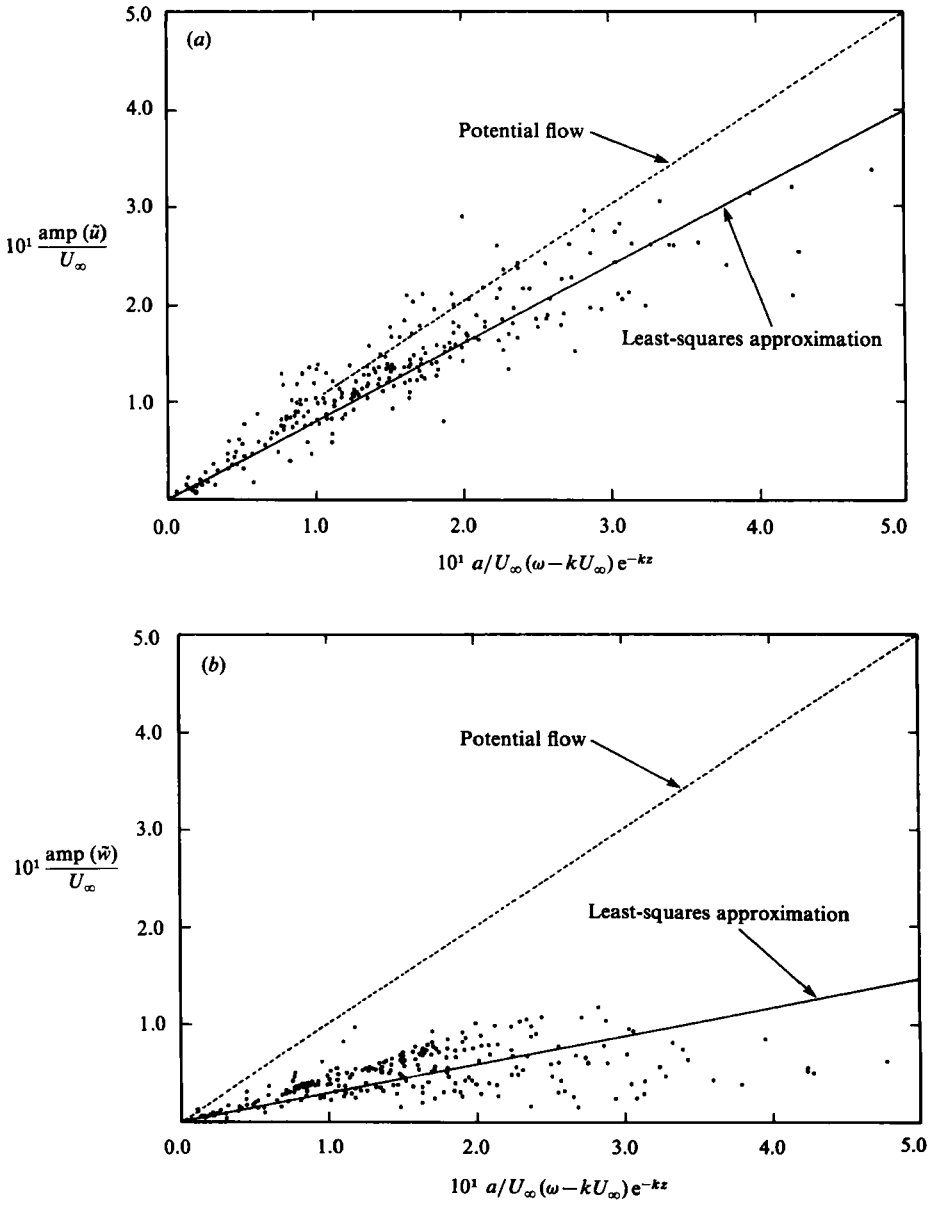

FIGURE 8. (*a*) The amplitude of the horizontal component of wave-induced velocity as a function of the potential flow solution. (*b*) The amplitude of the vertical component of wave-induced velocity as a function of the potential flow solution.

7. The wind–wave energy flux

The above results, together with (17), lead to a prediction of the air–water energy flux in an opposing wind. That $\phi_{\tilde{p}\eta} \approx 180°$ indicates that there is little significant air–water energy flux due to normal stresses, in contrast to a following wind, where there is a marked phase shift from 180°, and the normal stress is the dominant influence on wave growth. With $\overline{u''w''} \approx 0$ and neglecting the effects of viscous

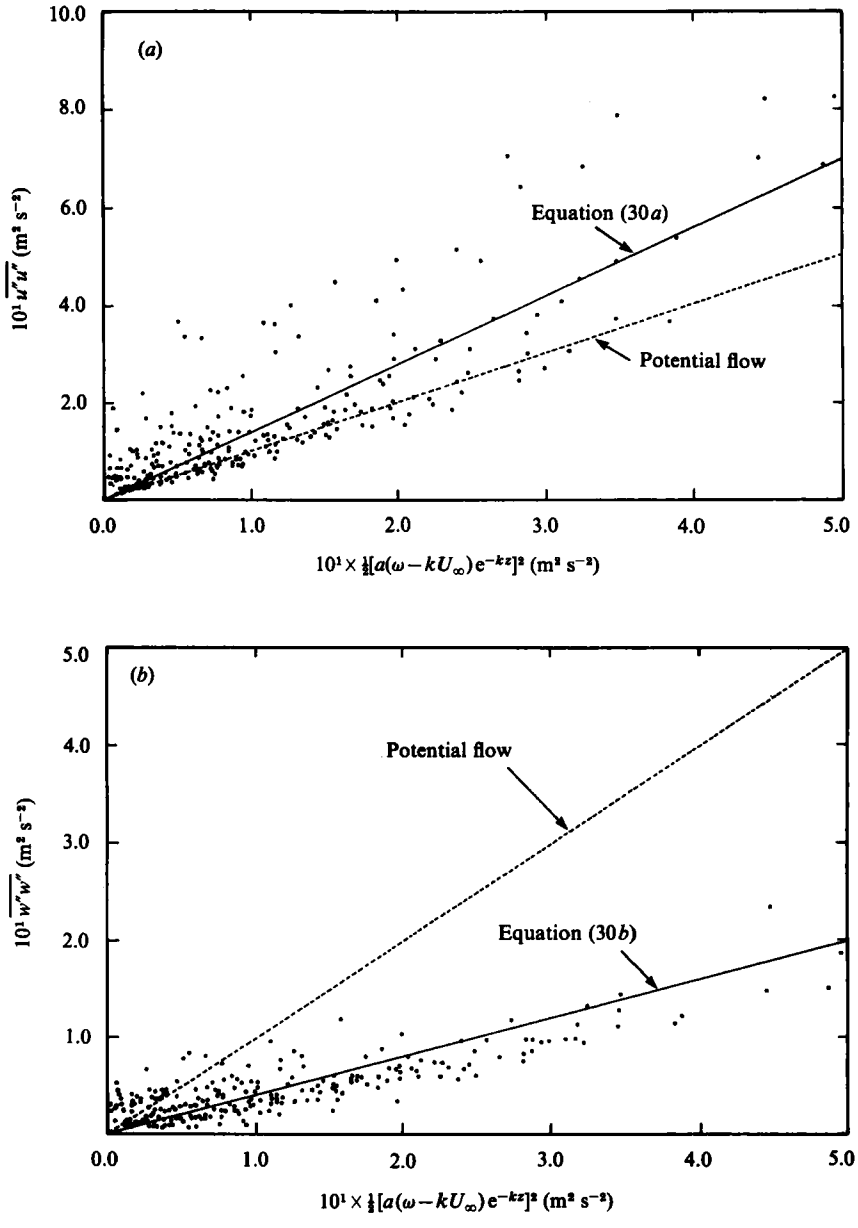

FIGURE 9*a*, *b*. For caption see page 440.

stresses, the only term contributing significantly to the air–water energy flux is $\overline{u''u''}$. Substituting (30*a*) for $\overline{u''u''}$ into (17) yields

$$\mu = (-0.7 \pm 0.2)\,(\rho_a/\rho_w)\,(ak)^2\,(1 - U_\infty/C)^2 \tag{31}$$

as an approximation to the coupling coefficient in an opposing wind.

Equation (31) is presented as a function of U_∞/C in figure 10 for various values of wave slope ak together with μ for a following wind as reported by Snyder *et al.* (1981). The strong dependence on the wave slope is clear; it is predicted that steep

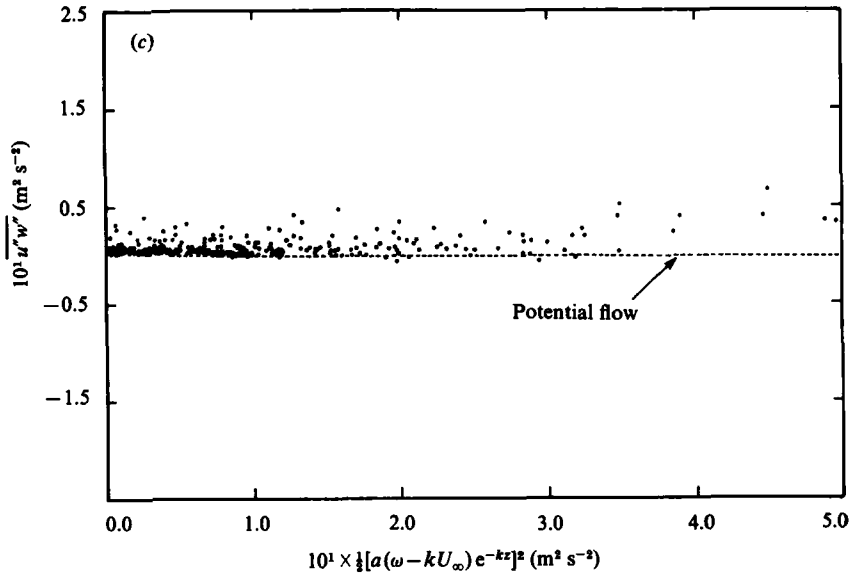

FIGURE 9. (*a*) The Reynolds stress term $\overline{u''u''}$ as a function of the potential flow solution. (*b*) The Reynolds stress term $\overline{w''w''}$ as a function of the potential flow solution. (*c*) The Reynolds stress term $\overline{u''w''}$ as a function of the potential flow solution.

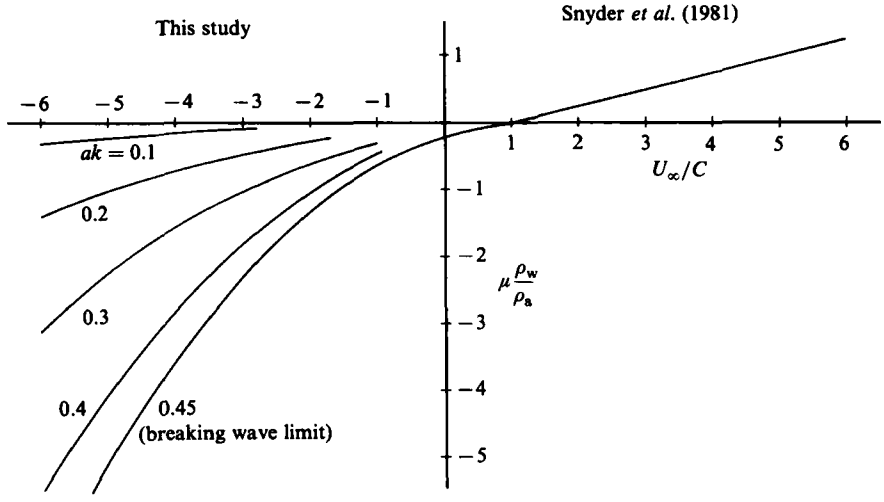

FIGURE 10. The wind–wave energy-flux coefficient μ as a function of U_∞/C and wave slope ak. The opposing-wind results are from (25) and are presented in conjunction with the following wind result of Snyder *et al.* (1981).

waves will be attenuated rapidly whereas less steep waves will remain almost unaffected by an opposing wind. Should a sudden reversal in wind direction confront a sea state containing both swell and locally generated wind sea, the high-frequency wind sea would be attenuated quickly but the swell would be almost unaltered.

Although reliable field data which could be used to corroborate these laboratory findings are rare, three useful data sets do exist, namely those by Snodgrass *et al.* (1966), Stewart & Teague (1980) and Snyder *et al.* (1981).

Snodgrass *et al.* (1966) observed the propagation of deep water waves across the Pacific Ocean from south of Australia past Hawaii to Alaska. For frequencies below 0.075 Hz, the waves decayed so slowly that the rate could hardly be measured. Above this frequency the decay rates were still very small but increased in magnitude with frequency. Although these waves would have encountered various local wind fields during their passage $U_\infty/C = 0$ might be a reasonable first approximation, in which case these results are consistent with (31). As an example, a swell component with $f = 0.05$ Hz, $H = 3$ m and $U_\infty/C = 0$ would be reduced in wave height by only 3% over a fetch of 15000 km (approximate propagation distance for the Snodgrass *et al.* experiment).

More comprehensive field measurements of wave decay in opposing winds have been obtained by Stewart & Teague (1980) who observed the growth and decay of approximately 0.14 Hz waves before and after the passage of a frontal system. The spectral variance of the waves was 0.093 m^2. The wind velocity was approximately 13 m s^{-1} and the wind shift was almost exactly 180°. Their measured growth rate was 6.7 times the decay rate. Assuming that the waves are sinusoidal, the wave amplitude is 0.43 m, the wave slope is 0.034 and $|U_\infty/C| = 1.17$. The Snyder *et al.* (1981) result for a following wind (figure 10) predicts $\mu = 0.034\rho_a/\rho_w$ for positive U_∞/C whereas (31) yields a corresponding decay rate of $\mu = -(0.0038 \pm 0.0011)\rho_a/\rho_w$; the growth rate is predicted to be between 6.9 and 12.6 times larger than the decay rate, compared with a value of 6.7 obtained by Stewart & Teague. Stewart & Teague actually measured the spectral evolution, which would also be influenced by wave–wave and wave–current interactions, so that their results are also in general agreement with (31).

The data of Snyder *et al.* (1981) provides some careful, though sparse, field measurements of the surface normal stress distribution for opposing winds. Their surface pressure and water-surface elevation measurements are essentially 180° out of phase, in agreement again with the predictions of potential flow theory and the present results.

8. Conclusions

An extensive set of laboratory experiments have determined the pressure and velocity fields above progressive water waves in an opposing wind. These results lead to a proposed source term for the radiative transfer equation that describes atmospheric transfer (decay) in an opposing wind.

The wave-induced pressure above the waves was approximately in antiphase with the water surface, consistent with the predictions of potential theory. It follows that there is no wind–wave energy flux due to quadrature pressure, in sharp contrast to that observed in following-wind situations, where the component of pressure in quadrature with the waves is the dominant source of the wind–wave energy flux. The magnitude of the wave-induced pressure fell below the potential theory predictions but still followed the same qualitative trend.

Measurements of the near-surface velocity field indicated that the wave-induced velocities $\tilde{u}$ and $\tilde{w}$ also followed the general trends expected for potential flow and that the normal Reynolds stress $-\rho_a \overline{u''u''}$ was the dominant source of wind–wave energy flux in an opposing wind. The predicted wave decay has a squared dependence on the wave slope and the ratio of the wind speed to the wave celerity. As a result, high-frequency waves will be attenuated much more rapidly than low-frequency waves.

This study was undertaken in the hydraulics laboratory of the Department of Civil and Systems Engineering, James Cook University, Townsville, Qld 4811, Australia, where the authors were respectively Research Officer and Reader in Civil Engineering.

REFERENCES

AMOROCHO, J. & DE VRIES, J. J. 1980 A new evaluation of the wind stress coefficient over water surfaces. *J. Geophys. Res.* **85**, 433–442.

CERMAK, J. E. 1971 Laboratory simulation of the atmospheric boundary layer. *AIAA J.* **9**, 1746–1754.

CHAO, S. P. & HSU, E. Y. 1978 Wave-induced velocities and turbulent Reynolds stress above an air–water interface. *Dynamics of Atmospheres and Oceans* **2**, 471–493.

DOBSON, F. W. 1971 Measurements of atmospheric pressure on wind-generated sea waves. *J. Fluid Mech.* **48**, 91–127.

ELLIOTT, J. A. 1972 Microscale pressure fluctuations near waves being generated by wind. *J. Fluid Mech.* **54**, 427–448.

HSU, C. T., HSU, E. Y. & STREET, R. L. 1981 On the structure of turbulent flow over progressive water waves: theory and experiment in a transformed wave-following co-ordinate system. *J. Fluid Mech.* **105**, 87–117.

LAMB, H. 1932 *Hydrodynamics.* Cambridge University Press.

LONGUET-HIGGINS, M. S. 1969 A nonlinear mechanism for the generation of sea waves. *Proc. R. Soc. Lond.* A **311**, 371–389.

MILES, J. W. 1957 On the generation of surface waves by shear flows. *J. Fluid Mech.* **3**, 185–204.

MILES, J. W. 1959 On the generation of surface waves by shear flows, Part 2. *J. Fluid Mech.* **6**, 568–582.

MILES, J. W. 1960 On the generation of surface waves by turbulent shear flows. *J. Fluid Mech.* **7**, 496–478.

MILES, J. W. 1962 On the generation of surface waves by shear flows, Part 4. *J. Fluid Mech.* **13**, 433–448.

MILES, J. W. 1967 On the generation of surface waves by shear flows, Part 5. *J. Fluid Mech.* **30**, 163–175.

PHILLIPS, O. M. 1957 On the generation of waves by turbulent wind. *J. Fluid Mech.* **2**, 417–445.

PHILLIPS, O. M. 1977 *The Dynamics of the Upper Ocean*, 2nd edn. Cambridge University Press.

SHEMDIN, O. H. 1969 Instantaneous velocity and pressure measurements above propagating waves. *Tech. Rep. No.* 4, *Dept. of Coastal and Oceanographic Engng, University of Florida.*

SIMIU, E. & SCANLAN, R. H. 1978 *Wind Effects on Structures: an Introduction to Wind Engineering.* Wiley.

SNODGRASS, F. E. *et al.* 1966 Propagation of ocean swell across the Pacific. *Phil. Trans. R. Soc. Lond.* A **259**, 431–497.

SNYDER, R. L. 1974 A field study of wave-induced pressure fluctuations above surface gravity waves. *J. Mar. Res.* **32**, 485–496.

SNYDER, R. L., DOBSON, F. W., ELLIOTT, J. A. & LONG, R. B. 1981 Array measurements of atmospheric pressure fluctuations above surface gravity waves. *J. Fluid Mech.* **102**, 1–59.

STEWART, R. H. & TEAGUE, C. 1980 Dekameter radar observations of ocean wave growth and decay. *J. Phys. Oceanogr.* **10**, 128–143.

WU, H. Y., HSU, E. Y. & STREET, R. L. 1977 The energy transfer due to air-input, nonlinear wave–wave interaction and white-cap dissipation associated with wind-generated waves. *Tech. Rep. No.* 207, *Dept of Civil Engng, Stanford University.*

YOUNG, I. R. 1983 The response of waves to an opposing wind. Ph.D. thesis, Department of Civil and Systems Engineering, James Cook University, Australia.